



Optimal Parameters for Maneuverability of Affordable Precision Munitions

by Frank Fresconi, Ilmars Celmins, and Luisa Fairfax

ARL-TR-5647

August 2011

NOTICES

Disclaimers

The findings in this report are not to be construed as an official Department of the Army position unless so designated by other authorized documents.

Citation of manufacturer's or trade names does not constitute an official endorsement or approval of the use thereof.

Destroy this report when it is no longer needed. Do not return it to the originator.

Army Research Laboratory

Aberdeen Proving Ground, MD 21005

ARL-TR-5647**August 2011**

Optimal Parameters for Maneuverability of Affordable Precision Munitions

Frank Fresconi, Ilmars Celmins, and Luisa Fairfax
Weapons and Materials Research Directorate, ARL

REPORT DOCUMENTATION PAGE				Form Approved OMB No. 0704-0188	
<p>Public reporting burden for this collection of information is estimated to average 1 hour per response, including the time for reviewing instructions, searching existing data sources, gathering and maintaining the data needed, and completing and reviewing the collection information. Send comments regarding this burden estimate or any other aspect of this collection of information, including suggestions for reducing the burden, to Department of Defense, Washington Headquarters Services, Directorate for Information Operations and Reports (0704-0188), 1215 Jefferson Davis Highway, Suite 1204, Arlington, VA 22202-4302. Respondents should be aware that notwithstanding any other provision of law, no person shall be subject to any penalty for failing to comply with a collection of information if it does not display a currently valid OMB control number.</p> <p>PLEASE DO NOT RETURN YOUR FORM TO THE ABOVE ADDRESS.</p>					
1. REPORT DATE (DD-MM-YYYY) August 2011		2. REPORT TYPE Final		3. DATES COVERED (From - To) January 2008 to October 2010	
4. TITLE AND SUBTITLE Optimal Parameters for Maneuverability of Affordable Precision Munitions				5a. CONTRACT NUMBER	
				5b. GRANT NUMBER	
				5c. PROGRAM ELEMENT NUMBER	
6. AUTHOR(S) Frank Fresconi, Ilmars Celmins, and Luisa Fairfax				5d. PROJECT NUMBER AH43	
				5e. TASK NUMBER	
				5f. WORK UNIT NUMBER	
7. PERFORMING ORGANIZATION NAME(S) AND ADDRESS(ES) U.S. Army Research Laboratory ATTN: RDRL-WML-E Aberdeen Proving Ground, MD 21005				8. PERFORMING ORGANIZATION REPORT NUMBER ARL-TR-5647	
9. SPONSORING/MONITORING AGENCY NAME(S) AND ADDRESS(ES)				10. SPONSOR/MONITOR'S ACRONYM(S)	
				11. SPONSOR/MONITOR'S REPORT NUMBER(S)	
12. DISTRIBUTION/AVAILABILITY STATEMENT Approved for public release; distribution unlimited.					
13. SUPPLEMENTARY NOTES					
14. ABSTRACT <p>High maneuverability of guided projectiles enables engagement of fleeing targets, opens the area of influence of a weapons system, and allows new missions to be performed such as prosecuting targets in defilade. Gun-launched precision munitions have unique constraints that create technical barriers to achieving enhanced maneuverability. Structural integrity during the gun launch event, packaging control surfaces within the launch tube, and affordability are paramount concerns. This work is a fundamental investigation of the flight mechanics and guidance, navigation, and control technologies necessary to optimize maneuverability of affordable precision projectiles. Detailed aerodynamic modeling and nonlinear equations of motion for the flight of a fin-stabilized airframe meeting low control authority constraints were simulated. Flight control laws were developed for various maneuver schemes with different actuator realizations. Simulations were conducted over a large parameter space to evaluate maneuverability. Results provide the optimal parameters within the distinctive scope of gun-launched munitions. Flying a skid-to-turn airframe with four canards in the "X" configuration maximizes control authority with moderate volume allocation and actuator bandwidth requirements. Examination of dynamic stability along with static stability illustrates that high-fidelity aerodynamic characterizations are required when optimizing maneuverability due to their impact on airframe design and flight control algorithm development.</p>					
15. SUBJECT TERMS projectile, guidance, maneuverability, control					
16. SECURITY CLASSIFICATION OF:			17. LIMITATION OF ABSTRACT UU	18. NUMBER OF PAGES 42	19a. NAME OF RESPONSIBLE PERSON Frank Fresconi
a. REPORT Unclassified	b. ABSTRACT Unclassified	c. THIS PAGE Unclassified			19b. TELEPHONE NUMBER (Include area code) (410) 306-0794

Contents

List of Figures	iv
List of Tables	v
1. Introduction	1
2. Aerodynamic and Flight Dynamic Modeling	2
3. Airframe	4
4. Maneuver Schemes and Actuator Types	5
5. Flight Control Laws	9
6. Simulation Parameters	13
7. Results	14
7.1 Ballistic Flight	14
7.2 Maneuver Flight	15
7.3 Static and Dynamic Stability	22
8. Conclusions	24
9. References	26
List of Symbols, Abbreviations, and Acronyms	28
Distribution List	30

List of Figures

Figure 1. Airframe in flight experiment.....	4
Figure 2. Pitching moment at Mach 0.7 for nominal, shifted center of gravity, and positive and negative deflections of pair of in-plane control surfaces.	5
Figure 3. Rolling airframe maneuver.....	6
Figure 4. Single-axis actuation of the two-canard rolling airframe scheme (left) and two-axis actuation of four-canard rolling airframe scheme (right).	7
Figure 5. Bank-to-turn maneuver.....	7
Figure 6. Two-axis actuation of four-canard skid-to-turn scheme.	8
Figure 7. Skid-to-turn maneuver.....	8
Figure 8. Three-axis actuation of the three-canard skid-to-turn scheme (left) and four-axis actuation of the four-canard skid-to-turn scheme (right).....	9
Figure 9. Roll angle history from the linear analysis.....	11
Figure 10. Roll rate angle history from the linear analysis.....	11
Figure 11. Deflection history from the linear analysis.	12
Figure 12. Root-locus for the roll controller.....	12
Figure 13. Ballistic downrange flight distance for the canard number and deploy time parameters.	14
Figure 14. Ballistic downrange flight distance for the canard number and quadrant elevation parameters.	15
Figure 15. Maneuver downrange flight distance for the maneuver scheme/actuator type and quadrant elevation parameters	16
Figure 16. Fractional increase in maneuver downrange flight distance for the maneuver scheme/actuator type parameter.....	17
Figure 17. Fractional increase in maneuver downrange flight distance for the actuation system volume parameter.	18
Figure 18. Fractional increase in maneuver downrange flight distance for the dimensionless glide start time and maneuver scheme/actuator type parameters.....	19
Figure 19. Fractional increase in maneuver downrange flight distance for the deployment time and dimensionless glide time parameters.	20
Figure 20. Fractional increase in the maneuver downrange flight distance for the control surface time constant and maneuver scheme/actuator type parameters.....	21
Figure 21. Fractional increase in the maneuver downrange flight distance for the center-of-gravity shift and maneuver scheme/actuator type parameters.	22
Figure 22. Dynamic stability for the center-of-gravity shift parameter.....	23

Figure 23. Coning motion obtained during an experimental flight of a rolling airframe with a damping rate of approximately $-0.0008/\text{m}$	24
---	----

List of Tables

Table 1. Projectile physical properties.	5
Table 2. Parameter space.	13

INTENTIONALLY LEFT BLANK.

1. Introduction

The guidance, navigation, and control (GNC) system has unique constraints for gun-launched precision munitions. Ensuring structural integrity of mechanical and electrical components during the gun launch event is difficult. Packaging requirements are stringent for the tube-launched environment. Fitting lifting surfaces within the launch tube often results in relatively small control surfaces as blades must be sub-caliber or stowed within the body (thereby competing with other subsystems for volume allocation). Finally, cost is a major driver in the development and production of precision systems. Expensive, high-performance actuators cannot be used on affordable systems. These aspects conspire to increase the technical difficulty for affordable precision projectiles. An example of these difficulties is achieving specified system accuracy requirements with reduced control effectiveness due to small lifting surfaces and poor actuators.

A few gun-launched precision munitions have been fielded or are currently in development for the U.S. Army (1–3). The GNC solutions for these systems address unique requirements and a general understanding of system parameters on maneuverability is unavailable in the literature. Extending the range of munitions by adding a control mechanism was investigated by Costello (4) and Fresconi (5). These efforts actively controlled the flight of a projectile but neither work exhaustively examined the airframe design or considered affordability or various maneuver schemes.

This work contributes to the field by identifying the fundamental relationships between maneuverability and maneuver scheme, actuator bandwidth, and airframe design under the unique constraints of the gun-launched projectile. The maneuverability of a canard-controlled, fin-stabilized projectile was considered in this study. Nonlinear flight dynamic simulations were conducted with well-characterized, realistic aerodynamics. Analysis of the effect of physical characteristics and aerodynamics of the airframe on the maneuverability was undertaken. Static stability was investigated by parametrically varying the location of the projectile's center of gravity. The control effectiveness of the candidate projectile was limited by relatively small lifting surfaces in accordance with the packaging constraints for gun-launched application. The deployment time after launch of the lifting surfaces was examined. The number of control surfaces depended on the maneuver scheme employed.

The maneuver schemes included rolling airframe, bank-to-turn, and skid-to-turn. A two-blade (single-axis) and four-blade (two-axis) actuation system was considered for the rolling airframe. For the non-rolling airframe, a four-blade (two-axis) bank-to-turn and both three-blade (three-axis) and four-blade (four-axis) skid-to-turn actuation systems were addressed. The four-blade bank-to-turn case flew in a “+” configuration of canards with respect to the gravity vector and the four-blade skid-to-turn case flew in an “X” configuration. Actuator bandwidth translates

directly into cost (i.e., higher bandwidth has higher cost); therefore, bandwidth requirements were quantified through a parametric study of the actuator time constant.

Flight control laws were derived for the different maneuver schemes. The purpose of the controllers was to maximize maneuverability through a range extension; therefore, the majority of the control effort was oriented opposite the gravity vector. The rolling airframe controller also mitigated projectile drift. Roll control and control surface mixing logic was used for the bank-to-turn and skid-to-turn schemes.

This report is organized as follows: the aerodynamic and flight dynamic model used for simulations is presented along with details on the airframe, followed by a description of the maneuver schemes, actuator types, and flight control laws, then results and conclusions.

2. Aerodynamic and Flight Dynamic Modeling

In the flight simulations, the aerodynamic forces and moments are broken into non-control (NC) and control (C) components. Aerodynamic symmetry is assumed for the NC components. The aerodynamic model for the NC components is presented in equations 1 and 2. These expressions contain coefficients for zero-yaw and yaw-squared axial force, normal force derivative, static roll moment, roll damping, pitching moment derivative, and pitch damping. All coefficients are functions of Mach number and some are functions of angle of attack. Specific functional dependencies of coefficients are included in parenthesis.

$$\begin{bmatrix} X_{NC} \\ Y_{NC} \\ Z_{NC} \end{bmatrix} = -QS \begin{bmatrix} C_X(M, \bar{\alpha}) \\ C_N(M, \beta) \\ C_N(M, \alpha) \end{bmatrix} \quad (1)$$

$$\begin{bmatrix} L_{NC} \\ M_{NC} \\ N_{NC} \end{bmatrix} = QSD \begin{bmatrix} C_{l_o}(M, \bar{\alpha}) + C_{l_p}(M) \frac{pD}{2V} \\ C_m(M, \alpha) + C_{m_q}(M) \frac{qD}{2V} \\ -C_m(M, \beta) + C_{m_q}(M) \frac{rD}{2V} \end{bmatrix} \quad (2)$$

The control force and moment models are generalized to any number of control surfaces at arbitrary locations on the projectile. Aerodynamic coefficients for the control surfaces are the axial force and normal force derivative. Additionally, the location of the center of pressure of the control surface is used to obtain control moments. Equations 3 and 4 show the summation of control forces and moments due to the i^{th} control surface. Note that dynamic pressure and angle of attack are calculated locally at each control surface. The local angle of attack for the i^{th} control surface is calculated as $\alpha_{C_i} = \arctan(w_{C_i}/u_{C_i}) + \delta_i$.

$$\begin{bmatrix} X_C \\ Y_C \\ Z_C \end{bmatrix} = \sum_{i=1}^{N_C} \begin{bmatrix} 1 & 0 & 0 \\ 0 & c_{\phi_{C_i}} & -s_{\phi_{C_i}} \\ 0 & s_{\phi_{C_i}} & c_{\phi_{C_i}} \end{bmatrix} Q_{C_i} S \begin{bmatrix} -C_{X_C}(M) \\ 0 \\ -C_{N_{\alpha C}}(M) \alpha_{C_i} \end{bmatrix} \quad (3)$$

$$\begin{bmatrix} L_C \\ M_C \\ N_C \end{bmatrix} = \sum_{i=1}^{N_C} \vec{r}_{CG \rightarrow CPC_i}(M) \times \begin{bmatrix} X_{C_i} \\ Y_{C_i} \\ Z_{C_i} \end{bmatrix} \quad (4)$$

The six degree-of-freedom model was employed for flight simulations (6, 7). The equations of motion are expressed in the body-fixed reference frame. The translational and rotation kinematics are given in equations 5 and 6:

$$\begin{bmatrix} \dot{x} \\ \dot{y} \\ \dot{z} \end{bmatrix} = \begin{bmatrix} c_{\theta} c_{\psi} & s_{\phi} s_{\theta} c_{\psi} - c_{\phi} s_{\psi} & c_{\phi} s_{\theta} c_{\psi} + s_{\phi} s_{\psi} \\ c_{\theta} s_{\psi} & s_{\phi} s_{\theta} s_{\psi} + c_{\phi} c_{\psi} & c_{\phi} s_{\theta} s_{\psi} + s_{\phi} c_{\psi} \\ -s_{\theta} & s_{\phi} c_{\theta} & c_{\phi} c_{\theta} \end{bmatrix} \begin{bmatrix} u \\ v \\ w \end{bmatrix} \quad (5)$$

$$\begin{bmatrix} \dot{\phi} \\ \dot{\theta} \\ \dot{\psi} \end{bmatrix} = \begin{bmatrix} 1 & s_{\phi} t_{\theta} & c_{\phi} t_{\theta} \\ 0 & c_{\phi} & -s_{\phi} \\ 0 & s_{\phi}/c_{\theta} & c_{\phi}/c_{\theta} \end{bmatrix} \begin{bmatrix} p \\ q \\ r \end{bmatrix} \quad (6)$$

Equations 7 and 8 provide the translational and rotational dynamics. The total forces and moments were found by adding the NC and C aerodynamic terms along with the force of gravity acting on the projectile.

$$\begin{bmatrix} \dot{u} \\ \dot{v} \\ \dot{w} \end{bmatrix} = \frac{1}{m} \begin{bmatrix} X \\ Y \\ Z \end{bmatrix} - \begin{bmatrix} 0 & -r & q \\ r & 0 & -p \\ -q & p & 0 \end{bmatrix} \begin{bmatrix} u \\ v \\ w \end{bmatrix} \quad (7)$$

$$\begin{bmatrix} \dot{p} \\ \dot{q} \\ \dot{r} \end{bmatrix} = \vec{I}^{-1} \begin{bmatrix} L \\ M \\ N \end{bmatrix} - \vec{I}^{-1} \begin{bmatrix} 0 & -r & q \\ r & 0 & -p \\ -q & p & 0 \end{bmatrix} \vec{I} \begin{bmatrix} p \\ q \\ r \end{bmatrix} \quad (8)$$

The dynamics of deflection of the control surfaces were modeled as a first-order system. In this manner, realistic control surface deflection histories were included and the influence of actuator bandwidth, in the form of the control surface time constant, was considered.

$$\tau \dot{\delta} + \delta = \delta_{CMD} \quad (9)$$

These models were implemented in Matlab and numerically integrated using an iterative step size solver.

3. Airframe

One important constraint for gun-launched precision munitions is that control surfaces are often small. This investigation directly addresses this constraint. The different maneuver schemes and actuator types considered in this effort require various numbers of control surfaces, from two to four. The planform area of the control surface is held constant for all cases. The aerodynamic and flight dynamic models enable analysis of these different numbers of control surfaces given quality aerodynamic coefficients. Aerodynamic characterizations of a precision munition meeting the low control authority constraint were undertaken using aeroprediction, wind tunnel testing, and flight experiments (8). An image of this projectile in a two-canard configuration is given in figure 1. The aerodynamic database for this projectile contains realistic features such as trims and nonlinearities with angle of attack and Mach number, which are essential for obtaining the most representative flight simulations. Rear fins are fixed in this effort; only nose-mounted canards are actively deflected in flight.



Figure 1. Airframe in flight experiment.

The physical properties for this projectile are provided in table 1. The center of gravity was varied from the nominal location to assess the influence of static stability on maneuverability and dynamic stability. The exterior shape (and thus aerodynamic force distribution) was held constant in accordance with the low control authority constraint. The pitching moment and control surface center of pressure with respect to the center of gravity were modified based on the center of gravity shift from the nominal location. In this effort, a positive shift in the center of gravity is toward the rear of the projectile (less static stability).

Table 1. Projectile physical properties.

Mass	44.1	kg
Diameter	155	mm
Length	981	mm
Center-of-gravity (nominal)	598	mm from nose
Axial inertia	0.167	kg-m ²
Transverse inertia	2.25	kg-m ²

A sample of the pitching moment coefficient is shown in figure 2. Nonlinearities in the angle of attack are evident. The effect of shifting the center of gravity ± 0.45 calibers (cal) is presented along with curves for deflecting a pair of control surfaces $\pm 10^\circ$.

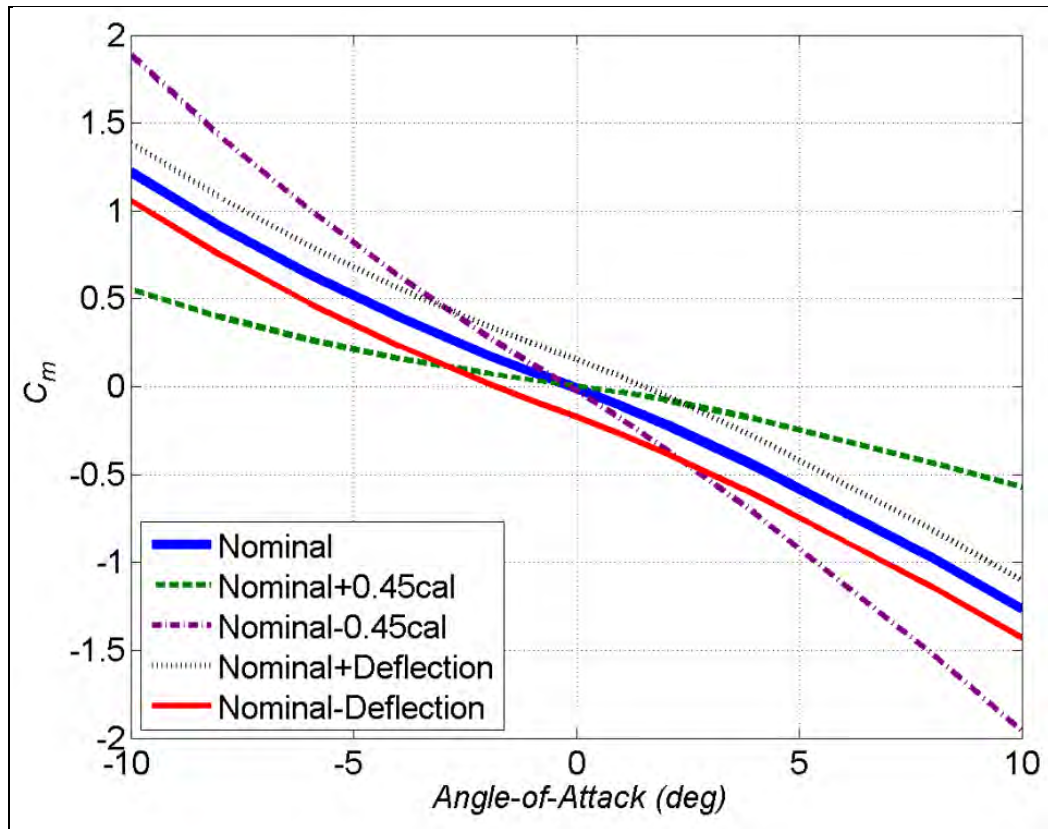


Figure 2. Pitching moment at Mach 0.7 for nominal, shifted center of gravity, and positive and negative deflections of pair of in-plane control surfaces.

4. Maneuver Schemes and Actuator Types

Three maneuver schemes were addressed: rolling airframe, bank-to-turn, and skid-to-turn. Maneuvering a rolling airframe is based on deflecting the control surfaces at the roll rate. This concept is illustrated in figure 3 for a two-control-surface configuration. When viewed from

behind the projectile at a roll orientation of 0° , control surfaces are deflected to provide a control force in the same direction to achieve maneuver. As the projectile rolls 90° , the control surfaces are undeflected since control force cannot be exerted in the desired direction. Control surfaces are deflected in a manner consistent with the initial (0° roll orientation) control force direction when the projectile rolls to 180° . Control surfaces are undeflected again at a roll angle of 270° . The sequence repeats at successive roll cycles. Any desired maneuver direction (e.g., up, down, left, right) is available by phase shifting the control surface deflection within the roll period.

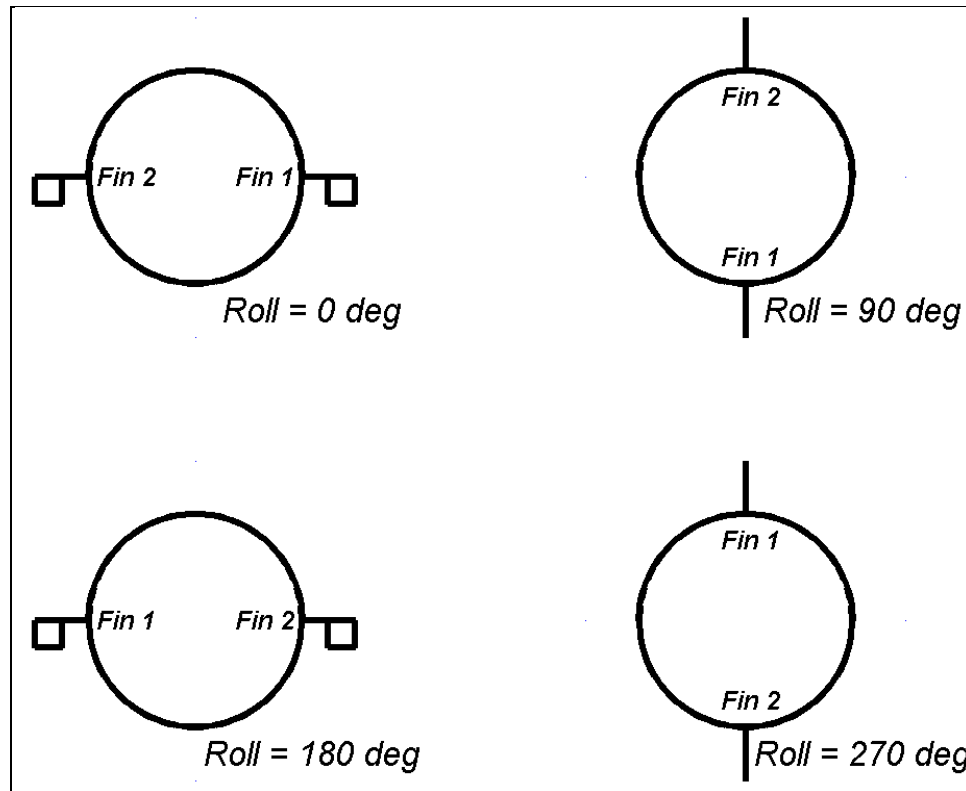


Figure 3. Rolling airframe maneuver.

The simplest (and most affordable) actuation of a rolling airframe with two control surfaces is a single-axis actuator driving both control surfaces simultaneously. Extending this idea farther, an N -axis actuator may drive $2N$ control surfaces to maneuver a rolling airframe. For practical packaging reasons, this study considers a two-axis actuator on a four-control-surface configuration of a rolling airframe in addition to the single-axis actuator with two control surfaces. Design of these two actuation systems for the rolling airframe scheme was undertaken and the solid model renderings are shown in figure 4. A linear voice coil, which has been experimentally rated past 20,000 times the acceleration of gravity, was used as the actuator. For the single-axis system, the linear voice coil is coupled through a mechanism, which produces the rotational motion of the canards. Miniaturizing the actuation system allows the control authority to be maximized by pushing the control surfaces as far toward the nose as possible. The two-axis system is essentially two single-axis actuation systems oriented with respect to each other

such that the appropriate configuration of canards is obtained. Considering the details of the actuator realization enables this study to address the volume allocation, location within the munition, and control surface stowing and deployment.

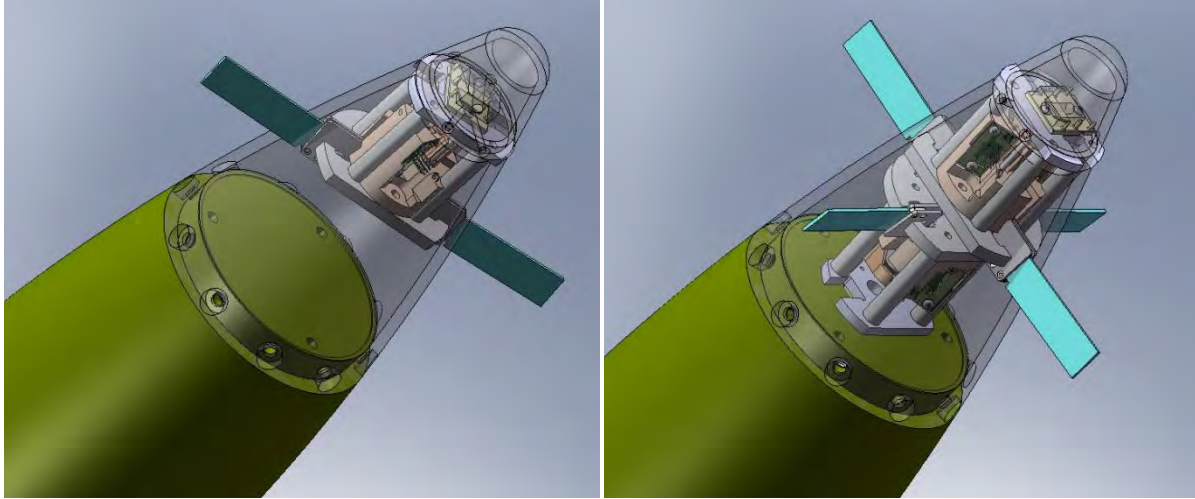


Figure 4. Single-axis actuation of the two-canard rolling airframe scheme (left) and two-axis actuation of four-canard rolling airframe scheme (right).

The bank-to-turn maneuver relies on a pair of control surfaces deflected in opposite directions to change roll orientation followed by a pair of control surfaces to achieve lateral maneuver once the desired roll orientation is achieved. This concept is illustrated in figure 5. At a roll angle of 0° , control surfaces 1 and 3 deflect in opposite directions to induce roll. As the projectile rolls to 90° , control surfaces 1 and 3 are undeflected and surfaces 2 and 4 deflect in the same direction for the lateral maneuver.

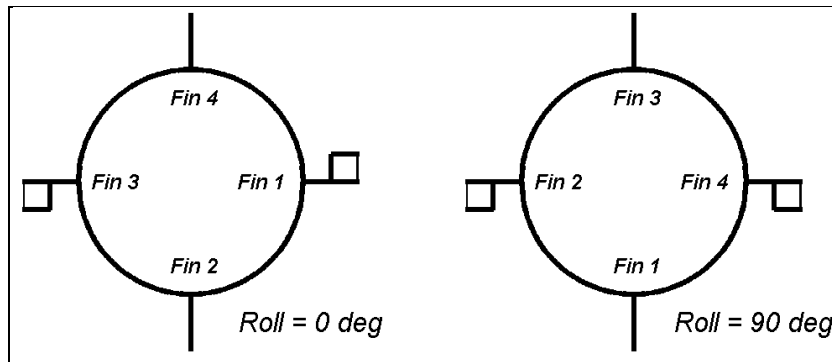


Figure 5. Bank-to-turn maneuver.

A two-axis actuator, with one axis coupling two roll control surfaces and one axis coupling two lateral control surfaces, is the simplest and most frequent realization of the bank-to-turn steering approach. This arrangement, flying in a “+” configuration, was adopted for this study. The actuation system developed for the bank-to-turn scheme is presented in figure 6. Two gun-hard, miniature servo-motors drive the canards. One servo-motor differentially deflects the canards

for roll control and the other servo-motor deflects canards in tandem to produce the lateral maneuver.

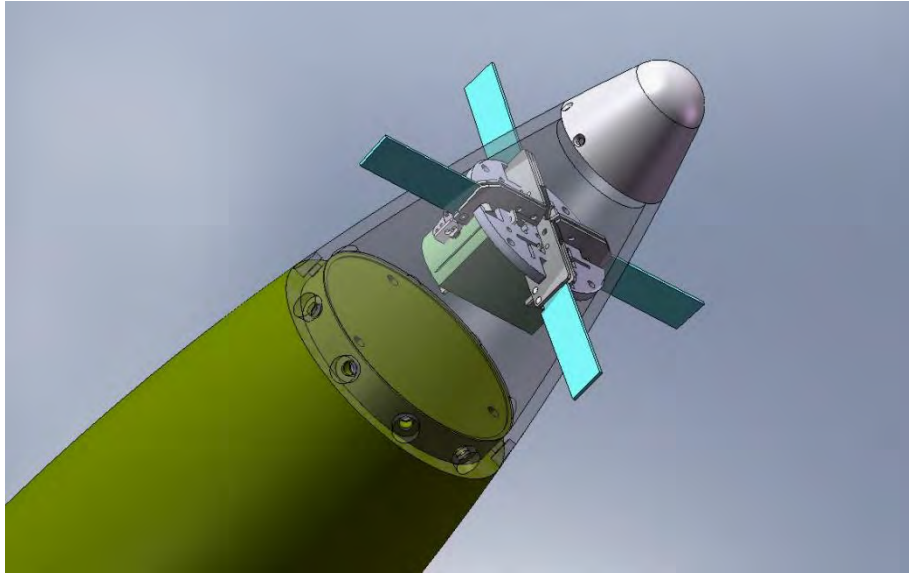


Figure 6. Two-axis actuation of four-canard skid-to-turn scheme.

Skid-to-turn maneuvering features each control surface performing roll control and lateral control simultaneously. In figure 7, the skid-to-turn scheme desires to perform a lateral maneuver in a given direction and keep the roll orientation such that the airframe flies in an “X” configuration. As such, the left-most illustration shows the projectile at -15° roll orientation so control surfaces 1 and 4 are deflected differently than control surfaces 2 and 3. A moment to roll into the “X” configuration results from the net differential control surface deflection. Furthermore, all surfaces produce a lateral force in a consistent direction so lateral control still takes place during the roll control. Once the desired roll orientation is achieved (right-most illustration in the figure), all surfaces deflect for lateral maneuver.

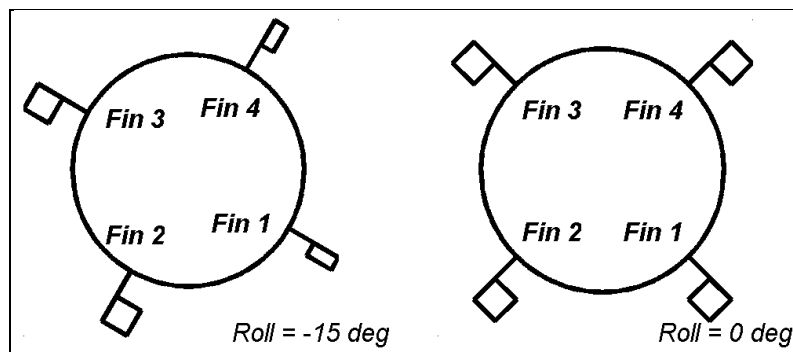


Figure 7. Skid-to-turn maneuver.

Independent actuators on each control surface are necessary for skid-to-turn maneuvering. In keeping with the affordability constraint of this effort, minimal skid-to-turn configurations

(three-axis/three control surfaces and four-axis/four control surfaces) were considered in this study. Solid model renderings of the actuation systems for the three- and four-axis configurations are provided in figure 8. The same servo-motor used for the bank-to-turn scheme was adopted for the skid-to-turn actuators. The four-axis/four control surface system flew in an “X” configuration.

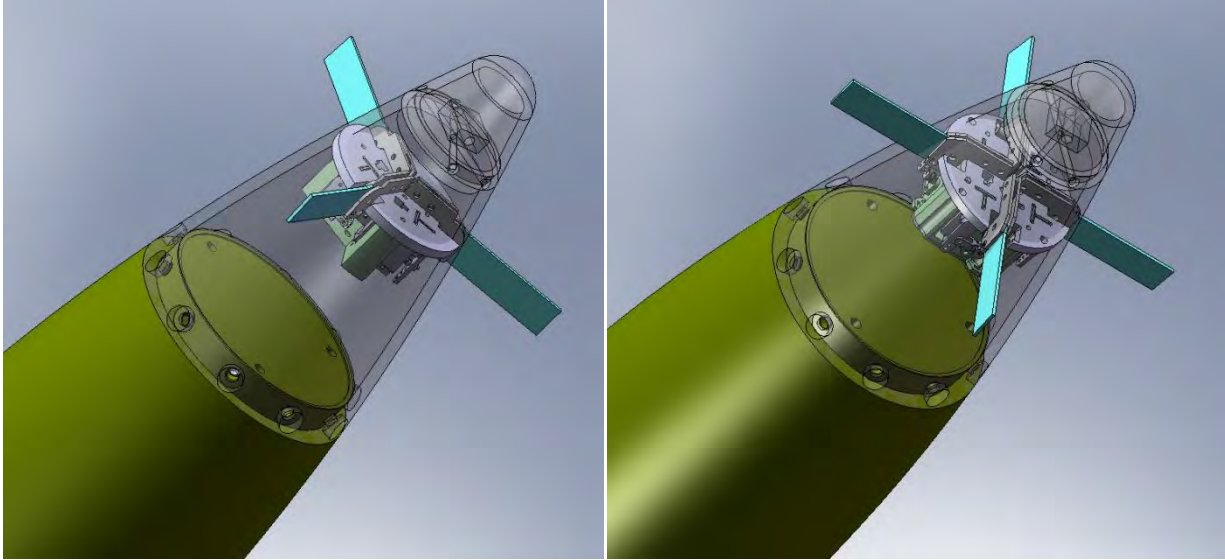


Figure 8. Three-axis actuation of the three-canard skid-to-turn scheme (left) and four-axis actuation of the four-canard skid-to-turn scheme (right)

5. Flight Control Laws

The goal of the flight control was to maximize the downrange flight distance in keeping with the given maneuver scheme. The rear fins had a fixed cant for the rolling airframe to roll the projectile during flight. Both two- and four-axis rolling airframes deflected each control surface to the maximum with a change in sign once per roll period to maintain the control force in a consistent direction (i.e., opposite the gravity vector). Projectile drift is a phenomenon that causes an increase in the crossrange (normal to line-of-fire) distance of the trajectory due to the interaction of gravity, spin, and pitching moment. Drift magnitude increases with spin rate and angle of attack. For gliding, a slowly rolling airframe’s angle of attack can be high enough to cause significant drift. To maximize downrange flight distance, drift must be mitigated. One method to reduce drift is to issue a slight phase-shift command in the desired maneuver orientation. This approach was developed by Fresconi (5). Using inertial position and velocity feedback in a simple controller was shown to effectively remove projectile drift and maximize downrange flight distance. The flight control law shown in equation 10 was used in this effort to determine where in the roll cycle to change the sign of the deflection for the rolling airframe scheme.

$$\phi_{CMD} = \arctan \left[\frac{K_{PG}(\psi - \psi_T) + K_{DG}(\dot{\psi} - \dot{\psi}_T)}{-(z - z_T)} \right] \quad (10)$$

Both bank-to-turn and skid-to-turn schemes featured rear fins without cant; however, launch conditions, manufacturing tolerances, and interactions and disturbances experienced during flight necessitate roll control. A general controller, using linear quadratic regulator control techniques, was developed for use in both schemes. Using linear quadratic regulators for roll control has been done in the past (9–11). The present formulation adds to the past work by including the fundamental flight dynamics of roll. Roll dynamics of a projectile are derived in Murphy (7). These equations can be modified slightly and expressed in state-space form ($\dot{\vec{x}} = \vec{A}\vec{x} + \vec{B}\vec{u}$) with $\vec{x} = [\phi \quad \dot{\phi}]^T$ and $\vec{u} = \delta_{CMD,i}$. The state transition and control matrices are shown in equations 11 and 12:

$$\vec{A} = \begin{bmatrix} 0 & 1 \\ 0 & \frac{QSD^2}{2VI_a} C_{lp} \end{bmatrix} \quad (11)$$

$$\vec{B} = \begin{bmatrix} 0 \\ \frac{QSDN_C}{I_a} C_{N\alpha C} \end{bmatrix} \quad (12)$$

The linear quadratic regulator expresses the control as $\vec{u} = -\vec{K}\vec{x}$, where the gain is given by equation 13 and \vec{P} can be found by solving the algebraic matrix Riccati equation shown in equation 14. The weightings for control effort and control error allow tuning of the controller for a given application. This roll controller is extensible to the two, three, and four control surfaces for different cases of the bank-to-turn and skid-to-turn schemes.

$$\vec{K} = \vec{R}^{-1} \vec{B}^T \vec{P} \quad (13)$$

$$\vec{A}^T \vec{P} + \vec{P} \vec{A} - \vec{P} \vec{B} \vec{R}^{-1} \vec{B}^T \vec{P} + \vec{Q}_{LQR} = 0 \quad (14)$$

Linear performance and stability analyses were conducted on the roll control algorithm. Typical results are shown in figures 9 through 12. For an initially perturbed system with roll angle at 30° and roll rate at 2 rad/s, the roll and roll rate histories are shown in figures 9 and 10 along with the control surface deflection history to achieve this performance in figure 11. Satisfactory response and steady-state error are illustrated in these results. The root-locus plot in figure 12 shows that the controller remains stable for all gains.

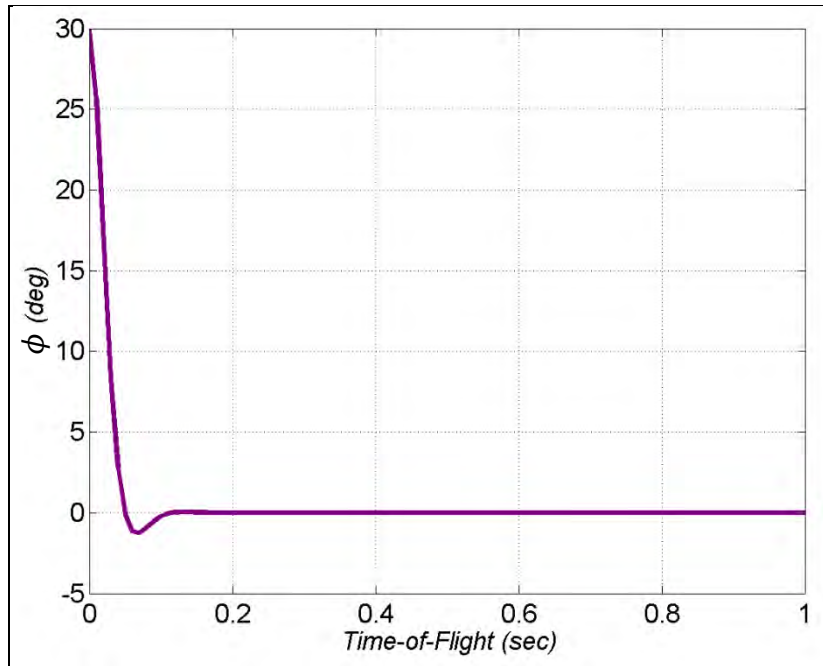


Figure 9. Roll angle history from the linear analysis.

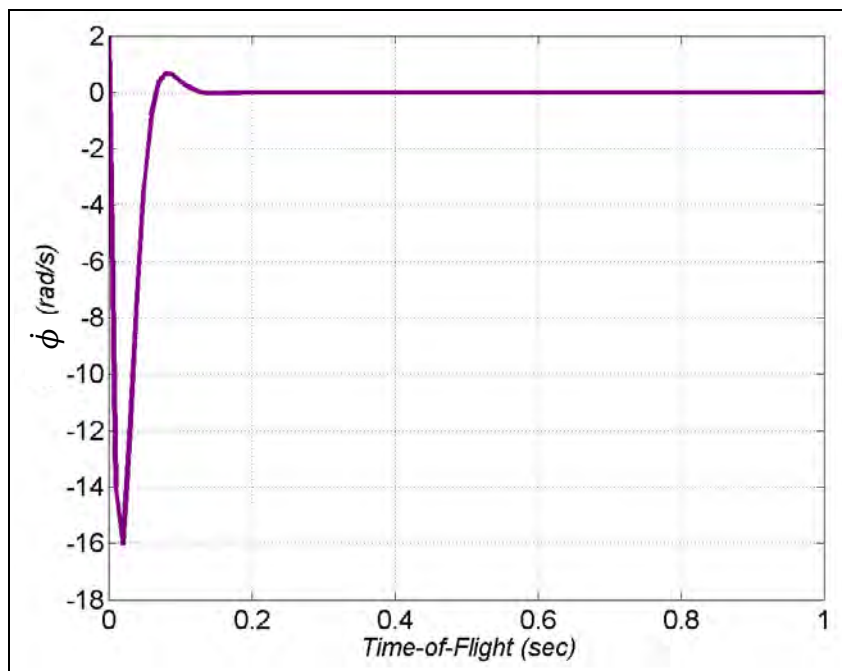


Figure 10. Roll rate angle history from the linear analysis.

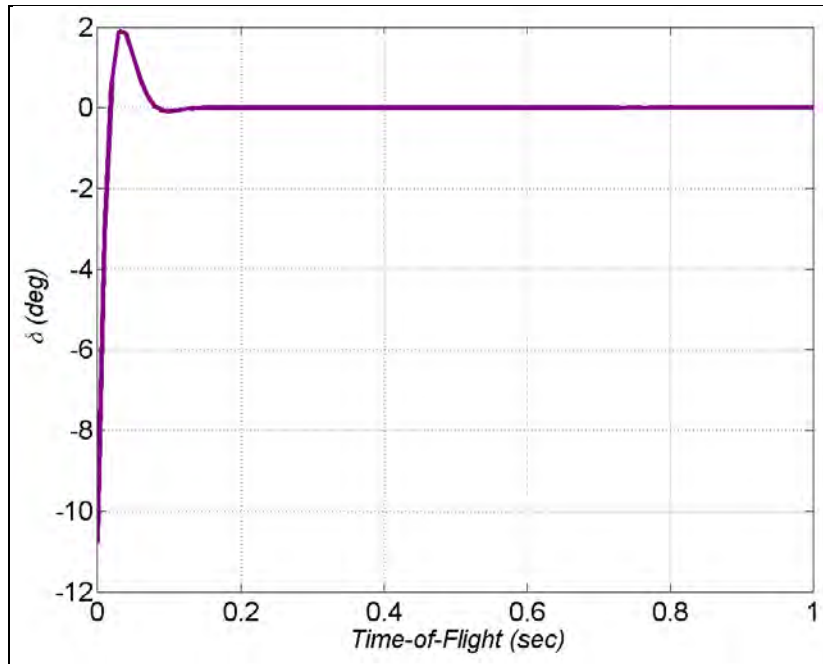


Figure 11. Deflection history from the linear analysis.

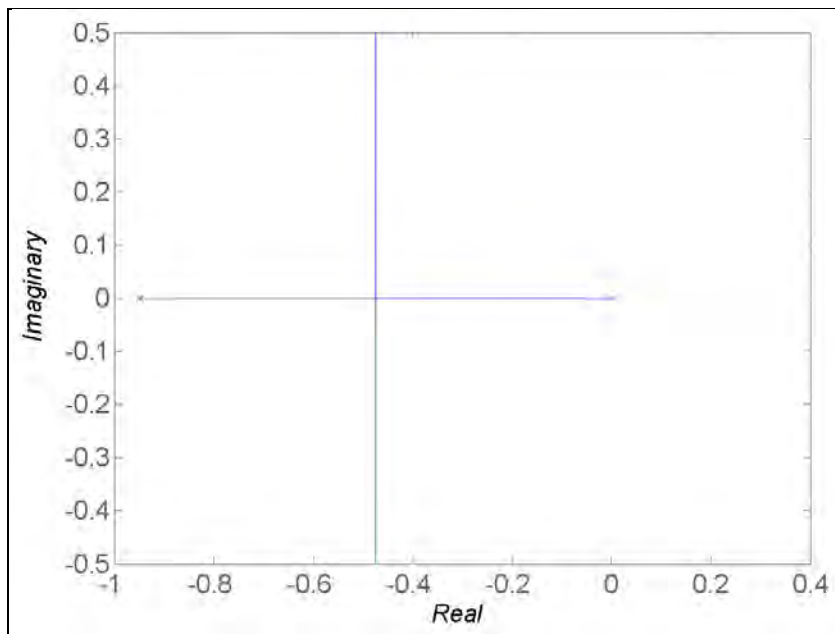


Figure 12. Root-locus for the roll controller.

The bank-to-turn scheme uses the roll controller to provide deflection commands for two control surfaces to keep the airframe in the “+” configuration. The other two control surfaces are deflected to the maximum throughout flight to maximize downrange flight distance.

Skid-to-turn deflection commands for the three- and four-axis system are generated by blending roll control with lateral maneuver for all control surfaces. The roll control algorithm outlined previously is used to determine roll deflection commands. The orientation of each control surface with respect to the desired lateral maneuver direction (opposite the gravity vector) is used to generate lateral maneuver deflection commands. The final skid-to-turn deflection command is produced simply by adding the de-coupled roll deflection command to the lateral maneuver deflection command.

Perfect state feedback was used. Limiters were placed on all deflection commands ($\pm 10^\circ$).

6. Simulation Parameters

The airframe was equipped with the flight control laws for the pertinent maneuver scheme and simulated using the equations of motion outlined previously. A parametric study was conducted to address the maneuverability as a function of the maneuver scheme, actuator bandwidth, and airframe design for the unique constraints of the gun-launched environment. The complete parameter space for the simulations is included in table 2.

Table 2. Parameter space.

Maneuver Scheme/Actuator Type	Quadrant Elevation ($^\circ$)	t_{deploy} (s)	t_{glide} (s)	τ (s)	Center-of-gravity shift (cal)
Rolling airframe - 2 control surfaces	35–60	0–45	25–55	0–0.1	–0.45–0.45
rolling airframe - 4 control surfaces					
Bank-to-turn - 4 control surfaces (+)					
Skid-to-turn - 3 control surfaces					
Skid-to-turn - 4 control surfaces (X)					

The launch velocity was 696 m/s. Downrange flight distance was the primary measure of performance for this effort.

7. Results

7.1 Ballistic Flight

Simulations were conducted to determine the baseline ballistic (non-maneuvering) downrange flight distance of various configurations of the airframe through a subset of the parameter space. The ballistic range is dependent upon the number of canards, canard deployment time, quadrant elevation, and rear fin cant (rolling or non-rolling airframe). These parameters were varied and the results are presented in figures 13 and 14.

Figure 13 shows the downrange flight distance for the rolling/non-rolling airframes with two, three, or four canards as a function of deployment time. These results are at the quadrant elevation, which provides maximum downrange distance. Yaw of repose is generated for the rolling airframes, which results in crossrange drift and less downrange distance. More canards add drag, which decreases the downrange distance. As deployment time occurs later in flight, the number of canards is less important as the additional canard drag has less effect on the trajectory.

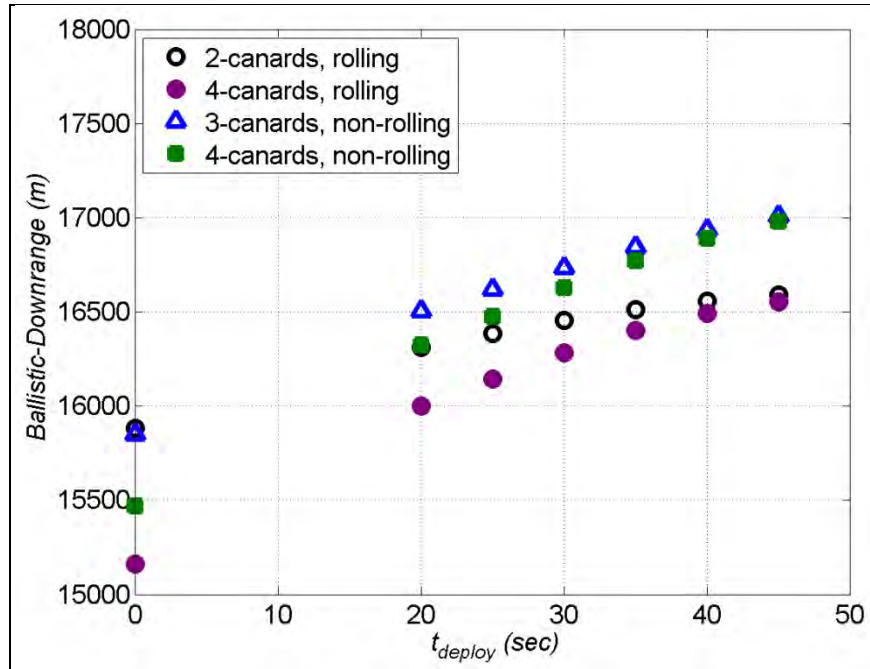


Figure 13. Ballistic downrange flight distance for the canard number and deploy time parameters.

Figure 14 illustrates the optimal quadrant elevation for ballistic flight is near 45° . Again, the rolling airframes encounter drift, which reduces the downrange distance, and more canards add drag, which also decreases downrange distance. These results are for the optimal deployment time.

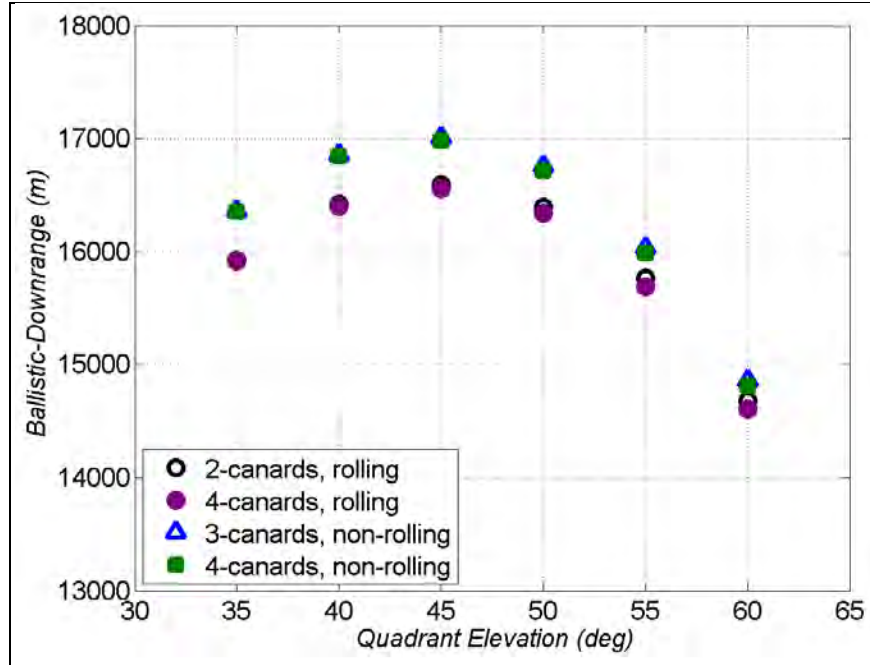


Figure 14. Ballistic downrange flight distance for the canard number and quadrant elevation parameters.

7.2 Maneuver Flight

Maneuver results are shown for the different parameters in figures 15 through 21. For each parameter under examination in the figures all other parameters are for the optimal (i.e., maximum downrange distance) configuration. In the legend of these figures, the maneuver scheme is denoted as “Rolling” for the rolling airframe, “BTT” for the bank-to-turn, and “STT” for the skid-to-turn, and the number of canards is represented with the relevant digit. The orientation of the canards during flight for the four control surfaces cases is differentiated with a “+” for the bank-to-turn scheme and an “X” for the skid-to-turn case.

As shown in figure 15, the optimal quadrant elevation for maneuver flight is different than that for ballistic flight. Furthermore, the optimal quadrant elevation is specific to the parameters such as maneuver scheme. For example, inherently higher maneuverability arrangements, such as the skid-to-turn case with four canards in the “X” configuration, need a steeper quadrant elevation to reach a higher altitude from which to pull a more favorable glide slope.

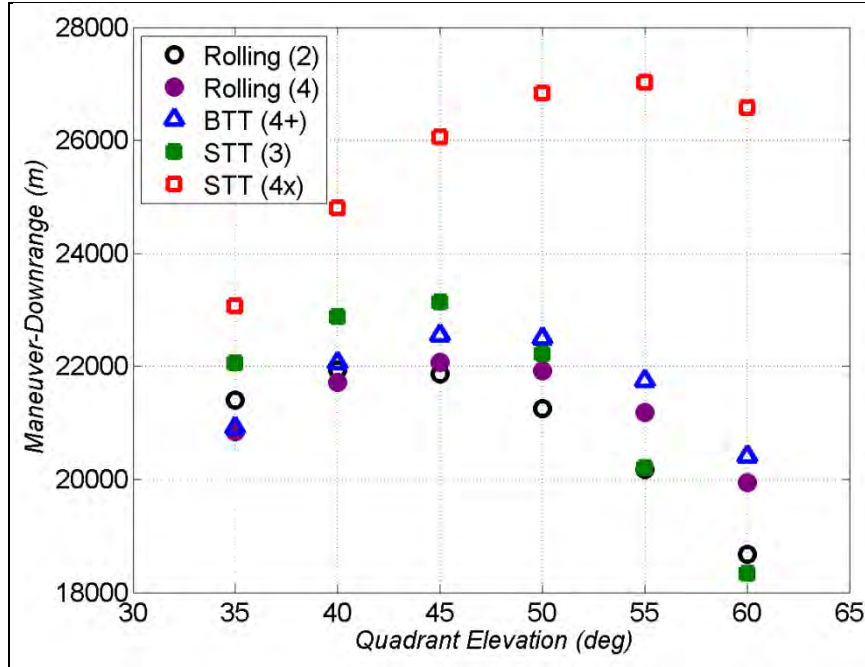


Figure 15. Maneuver downrange flight distance for the maneuver scheme/actuator type and quadrant elevation parameters

The following results have been expressed not as a downrange distance but as a dimensionless fractional increase of the maneuver downrange distance divided by the ballistic downrange distance. This metric provides some sense for the downrange increase due to active maneuvers. For all cases, the ballistic downrange distance used in the nondimensionalization was for the set of parameters that yielded the maximum downrange distance.

Comparing the different maneuver schemes/actuator types in figure 16 shows that only the skid-to-turn scheme with four canards in the “X” configuration significantly outperforms all others. This configuration flies about 75% farther than the maximum ballistic downrange distance while all other cases fly closer to 40% farther than the respective ballistic downrange distance. When the actuator bandwidth is considered (blue bars in figure 16), some disadvantages of the rolling airframe become apparent. While the specific roll rate of the airframe is important, it seems that in general rolling airframes may require higher bandwidth actuators to achieve the maximum possible maneuverability.

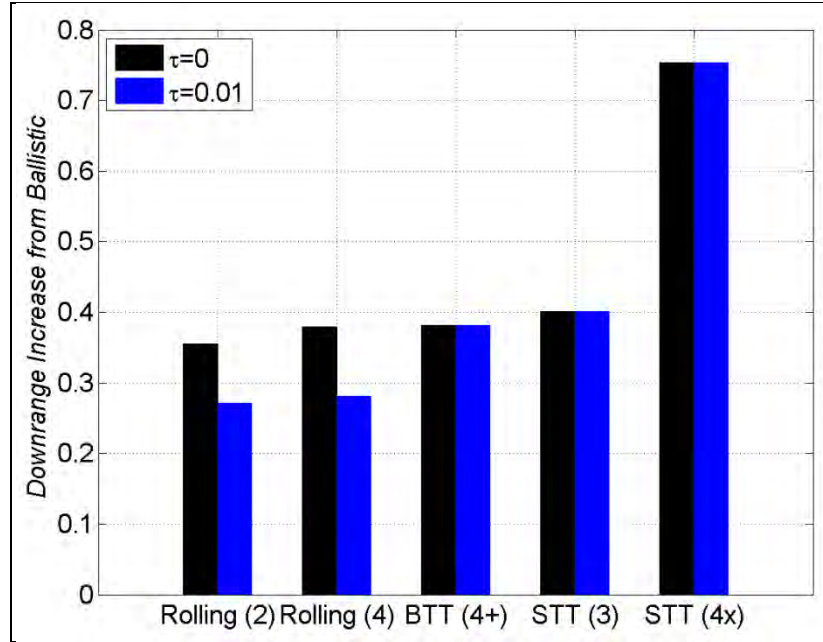


Figure 16. Fractional increase in maneuver downrange flight distance for the maneuver scheme/actuator type parameter.

To fully appreciate the trade-offs associated with various maneuver schemes/actuator types, the volume occupied by each actuation system was calculated. The volume of each system is relatively similar (approximately 110–165 cm³) except for the rolling airframe with four canards, which is twice the volume of the rolling airframe with two canards. Figure 17 presents the maneuverability as a function of the actuator volume. The skid-to-turn scheme flying with four canards in the “X” configuration has the best maneuverability and moderate (136 cm³) volume requirements. The bank-to-turn and skid-to-turn schemes with three canards feature the next most favorable maneuverability per unit actuation system volume.

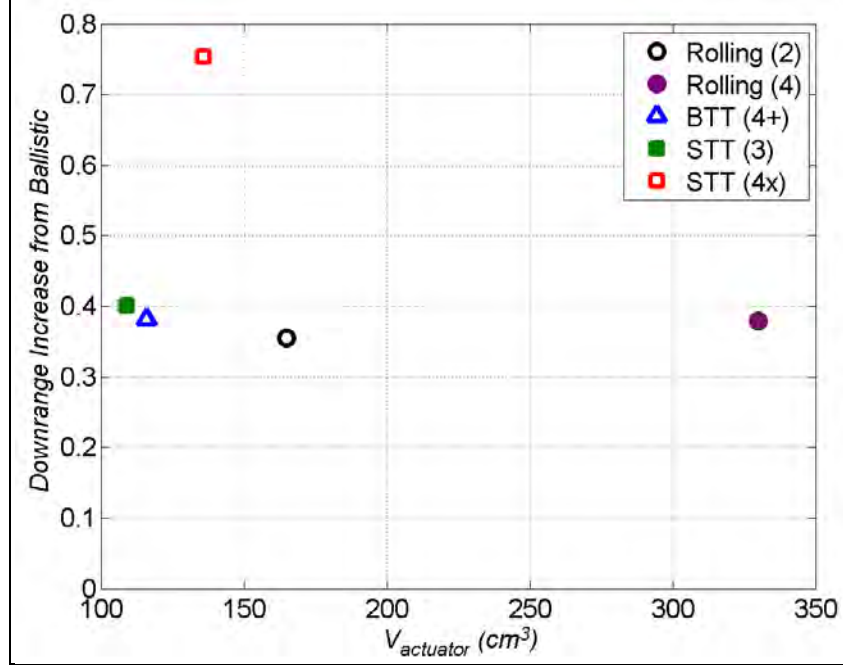


Figure 17. Fractional increase in maneuver downrange flight distance for the actuation system volume parameter.

The dependence of maneuverability on the glide start time is given in figure 18. Glide time was nondimensionalized by the total time of flight ($t_{glide}^* = t_{glide}/t_{flight}$). The optimal glide start time is near 25–30% into the flight depending on the configuration. This optimal glide time usually corresponded closely with apogee.

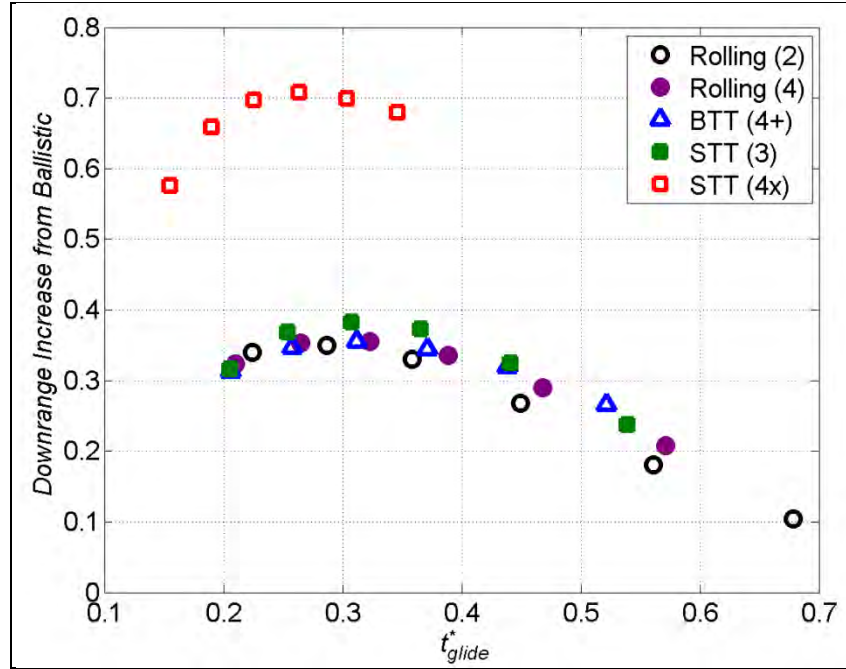


Figure 18. Fractional increase in maneuver downrange flight distance for the dimensionless glide start time and maneuver scheme/actuator type parameters.

The influence of canard deployment time on maneuverability is presented in figure 19. The skid-to-turn scheme with four canards in the “X” configuration is not shown so that a more zoomed in scale can be used. Maneuverability is insensitive to canard deployment time for this airframe. For example, the square symbols representing the skid-to-turn scheme with three canards deployed at the optimal time during flight is only a few percent better than the diamond symbols denoting the skid-to-turn scheme with three canards fixed (deployed) from launch. In contrast to the ballistic results (figure 13), when maneuver is considered the drag of the canards is mitigated by the lift produced.

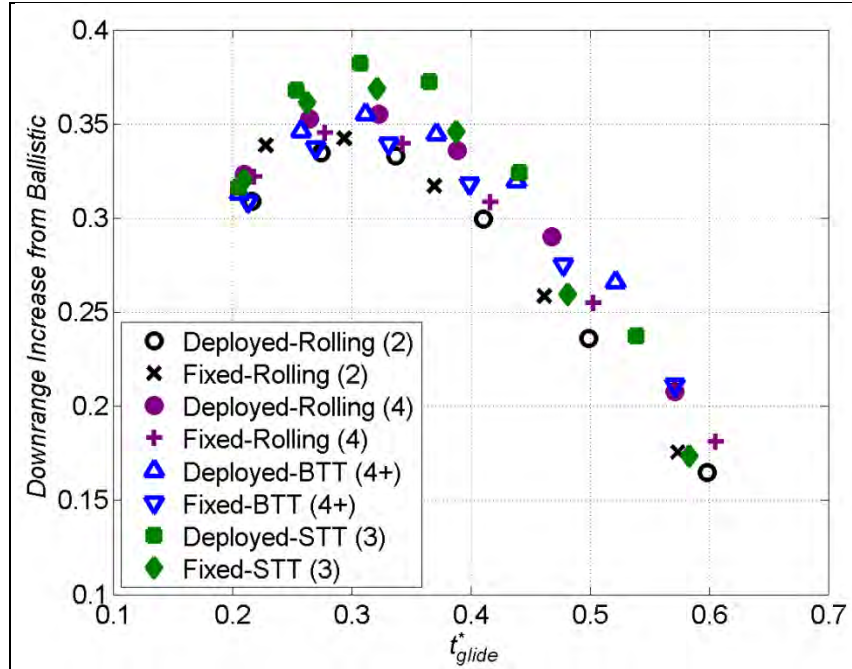


Figure 19. Fractional increase in maneuver downrange flight distance for the deployment time and dimensionless glide time parameters.

Actuator bandwidth often translates directly to cost and affordability is a driving factor in the fielding of precision munitions. Figure 20 shows the maneuverability of the different maneuver schemes/actuator types as a function of actuator bandwidth. The frequency at which these curves fall off for each case provides some sense for bandwidth requirement. Obviously, the rolling airframe needs the highest bandwidth ($\sigma \sim 1000$ Hz) although this is dependent on roll rate. The airframe in this effort had a roll rate between 10 and 30 Hz. The skid-to-turn scheme has the next highest bandwidth requirement ($\sigma \sim 100$ Hz) due to the need to perform roll and lateral control for each control surface simultaneously. The lowest bandwidth actuator requirements are for the bank-to-turn scheme, since the roll control axis can slowly orient the lateral control surfaces in the proper direction with little impact to the overall maneuverability.

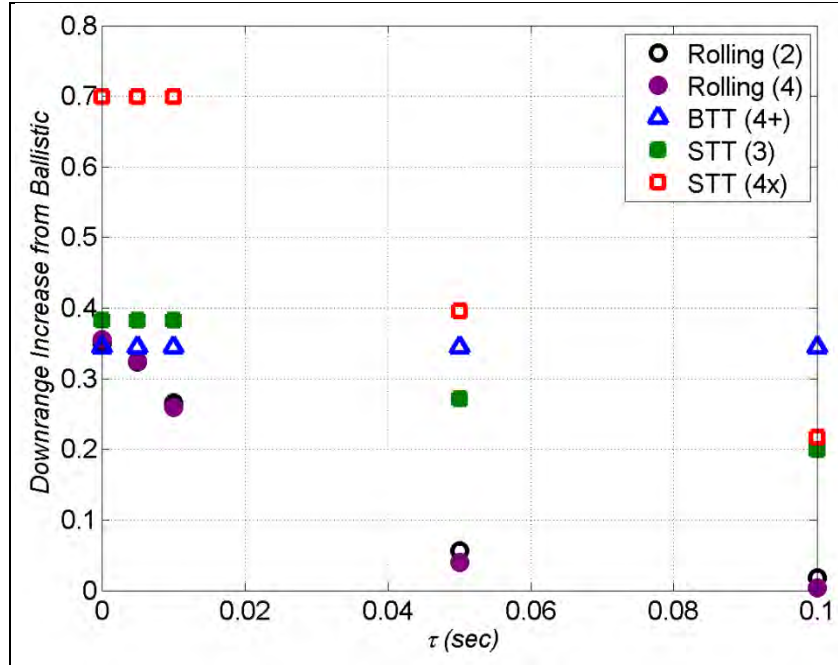


Figure 20. Fractional increase in the maneuver downrange flight distance for the control surface time constant and maneuver scheme/actuator type parameters.

Shifting the center of gravity, as shown in figure 21, has a large effect on maneuverability. Static stability dictates the control-induced angle of attack at which the airframe is able to glide. As this moment arm goes to zero, the maneuverability of all cases increases drastically. Beyond a center-of-gravity shift of 0.45 cal, this airframe is statically unstable at launch and throughout a majority of the flight.

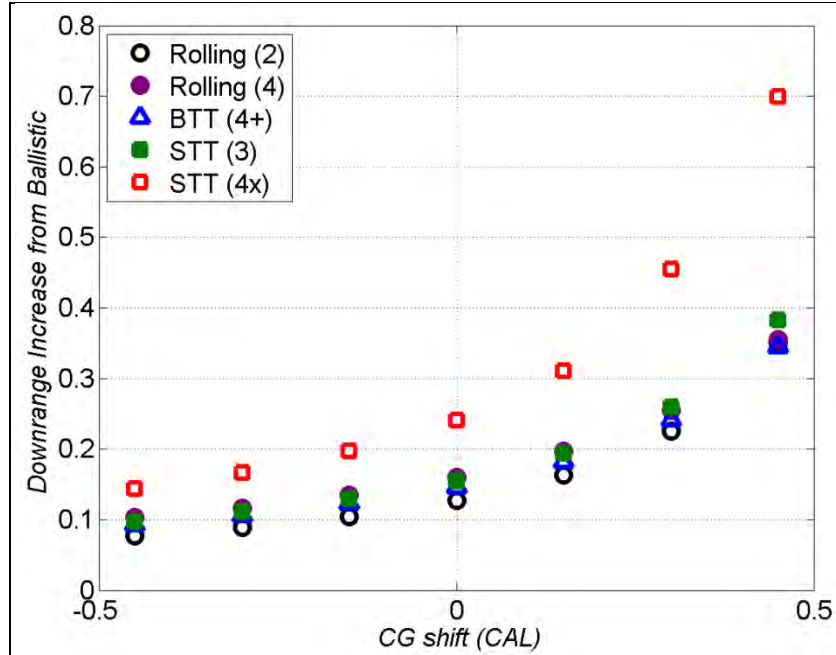


Figure 21. Fractional increase in the maneuver downrange flight distance for the center-of-gravity shift and maneuver scheme/actuator type parameters.

7.3 Static and Dynamic Stability

Designing a highly maneuverable precision munition by dialing in a low static margin must be tempered with a consideration of dynamic stability. Flight stability is often evaluated for projectiles using linear theory (6–7). This theory characterizes the angular motion of the projectile as an exponentially damped sinusoid. Stability is inferred directly by the damping rate; positive damping rate implies yaw growth (dynamic instability) and negative damping rate implies perturbations in angular motion decrease in amplitude (dynamic stability).

The physical properties and aerodynamics of the airframe used in this investigation were implemented in the linear theory calculations to obtain the damping rates at Mach 0.7 as a function of static stability, as shown in figure 22. The open circles show that the damping rate is negative (dynamic stability) for all values of static stability when no static side moment is present. Flight experiments conducted with this airframe identified a static side moment (8). When this aerodynamic term is added to the linear stability calculation, a dynamic instability (positive damping rate) occurs for low static stability.

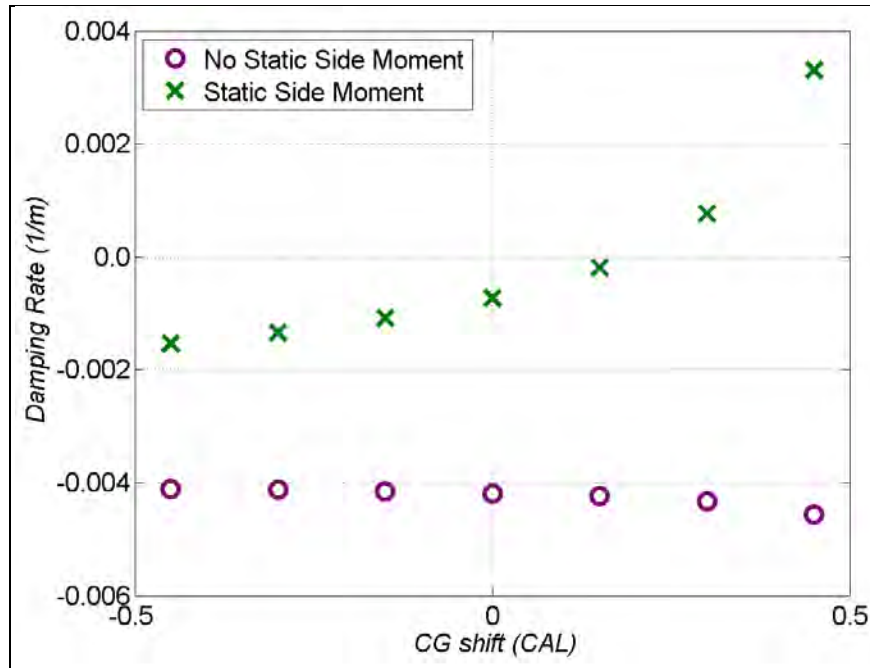


Figure 22. Dynamic stability for the center-of-gravity shift parameter.

Figure 23 was added to provide some sense for how a given damping rate maps into angular motion. Trajectory reconstruction was undertaken of an experimental flight of the airframe used in this study in a configuration with a rolling airframe composed of two canards. The 2° – 3° magnitude of coning motion obtained during the experimental flight shown in figure 23 corresponds to the static side moment curve with the center-of-gravity shift of zero (damping rate of approximately $-0.008/\text{m}$) in figure 22. This consideration of static and dynamic stability illustrates that realistic aerodynamic effects such as trims, static side moments, and dynamic side moments, which are often difficult to characterize with preliminary design tools, can have a significant impact to the airframe design and flight control algorithms.

Sensors such as high-grade accelerometers and gyroscopes may be used to provide stability through an active feedback loop for flight regimes where dynamic instabilities may exist. This approach adds cost. A more affordable precision munition solution should exclude the expensive inertial measurement unit and use a global positioning system (GPS) alone for state feedback and ensure dynamic stability through proper airframe design and characterization (13).

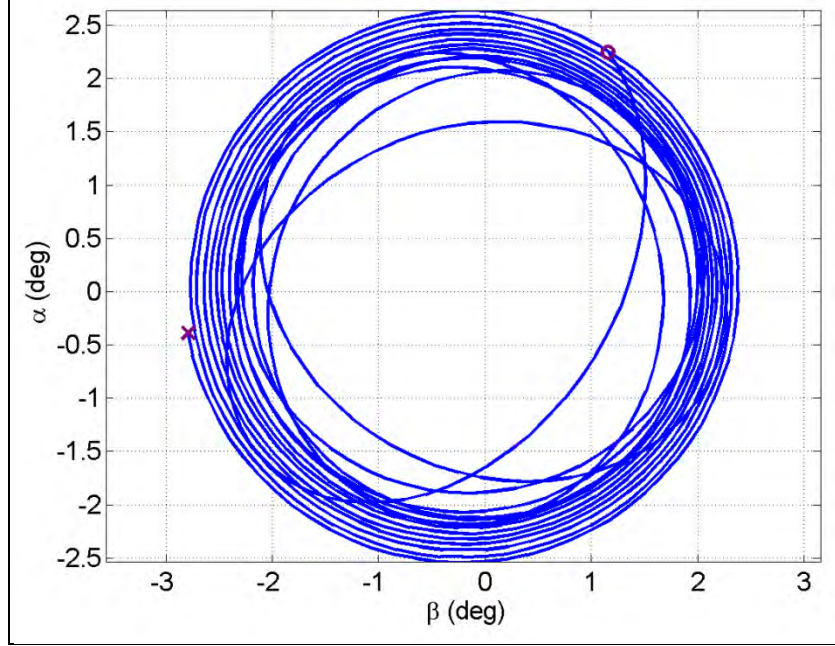


Figure 23. Coning motion obtained during an experimental flight of a rolling airframe with a damping rate of approximately $-0.0008/\text{m}$.

8. Conclusions

Dynamic modeling and simulation of the flight and control surface response of a guided projectile were performed in this effort. The aerodynamic database encompassed realistic effects such as trims, nonlinearities, and side moments, which increase the fidelity of the simulations. The airframe under investigation met the gun-launched precision munition constraint of weak control effectiveness. The design of the airframe in terms of static stability and maneuver scheme was examined. The three conventional maneuver schemes were addressed for different levels of actuator complexity. Besides the number of actuator axes required, the affordability of the maneuver system was also addressed through a bandwidth parameter. Flight control laws were developed to maximize maneuverability for the rolling airframe, bank-to-turn, and skid-to-turn schemes. A parametric study addressed the influence of quadrant elevation, glide start time, control surface deployment time, maneuver scheme/actuator type, and stability on the maneuverability of precision munitions.

The results indicate that a skid-to-turn scheme flying in the “X” configuration with four canards yields the most control authority. This configuration may feature moderate volume allocation and bandwidth requirements. Maneuverability was largely independent of the four other maneuver schemes/actuator types, provided the actuator bandwidth is high enough for the rolling airframes. Implications of realistic aerodynamic effects on the static and dynamic stability must

be considered. This finding entails early, high-fidelity flight characterizations. Post-launch deployment of control surfaces may be unnecessary from a maneuverability perspective and decrease technical risk but mandatory from a storage and handling viewpoint. Finally, given a specific configuration, simultaneous optimization of quadrant elevation and glide start time are needed to maximize maneuverability.

These results provide original and valuable insight into the optimal parameters for maneuvering guided munitions. Gun-launched precision projectiles have unique constraints on survivability, packaging, and affordability. Control surfaces are often small and actuators may be poor performing to meet some of these requirements. This fundamental investigation addresses optimal maneuverability in this distinctive environment.

9. References

1. Morrison, P. H.; Amberntson, D. S. Guidance and Control of a Cannon-launched Guided Projectile. *Journal of Spacecraft and Rockets* **1977**, 14 (6), 328–334.
2. Grubb, N. D.; Belcher, M. W. Excalibur: New Precision Engagement Asset in the Warfight. *Fires* **Oct.–Dec. 2008**, 14–15.
3. Moorhead, J. S. Precision Guidance Kits (PGKs): Improving the Accuracy of Conventional Cannon Rounds. *Field Artillery* **Jan.–Feb. 2007**, 31–33.
4. Costello, M. Extended Range of a Gun Launched Smart Projectile Using Controllable Canards. *Shock and Vibration* **2001**, 8, 203–213.
5. Fresconi, F. Range Extension of Gun-Launched Smart Munitions. *Proceedings of the 24th International Symposium on Ballistics*, New Orleans, LA, September 22–26, 2008, pp. 157–164.
6. Nicolaides, J. *On Missile Flight Dynamics*; Catholic University of America, Ph.D dissertation, 1963.
7. Murphy, C. *Free Flight of Symmetric Missiles*; Ballistics Research Lab. Rept. BRL-1216; Aberdeen Proving Ground, MD, 1963.
8. Fresconi, F.; Harkins, T. Aerodynamic Characterizations of Asymmetric and Maneuvering 105mm, 120mm, and 155mm Fin-Stabilized Projectiles Derived from Telemetry Experiments. *AIAA Atmospheric Flight Mechanics Conference*, August 2011.
9. Talole, S. E.; Godbole, A. A.; Kolhe, J. P.; Phadke, S. B. Robust Roll Autopilot Design for Tactical Missiles. *Journal of Guidance, Control, and Dynamics* **2011**, 34 (1), 107–117.
10. Nesline, F. W.; Wells, B. H.; Zarchan, P. Combined Optimal/Classic Approach to Robust Missile Autopilot Design. *Journal of Guidance, Control, and Dynamics* **1981**, 4 (3), 316–322.
11. Nesline, F. W.; Zarchan, P. Why Modern Controllers Can Go Unstable in Practice. *Journal of Guidance, Control, and Dynamics* **1984**, 7 (4), 495–500.
12. Cooper, G.; Costello, M.; Fresconi, F.; DeSpirito, J.; Celmins, I. Flight Stability of Asymmetric Projectiles with Control Mechanisms. *AIAA*, Paper No. 2010-7636, August 2010.

13. Fresconi, F.; Brown, T.; Celmins, I.; DeSpirito, J.; Ilg, M.; Maley, J.; Magnotti, P.; Scanlan, A.; Stout, C.; Vazquez, E. Very Affordable Precision Projectile System and Flight Experiments. *Proceedings of the 27th Army Science Conference*, Orlando, FL, 2010.

List of Symbols, Abbreviations, and Acronyms

$\alpha, \beta, \bar{\alpha}$	pitch, yaw, total angle-of-attack
ϕ_C	roll orientation of control surface
$\delta, \dot{\delta}$	control surface deflection, time rate of change of control surface deflection
δ_{CMD}	commanded control surface deflection
τ	time constant of control surface deflection
ϕ_{CMD}	roll command for drift controller
ϕ, θ, ψ	Euler angles
$\dot{\phi}, \dot{\theta}, \dot{\psi}$	time rate of change of Euler angles
\bar{A}, \bar{B}	state transition and controls matrix
C	control
C_{l_0}	static roll moment coefficient
C_{l_p}	roll damping coefficient
C_N	normal force coefficient
$C_{N_{\alpha C}}$	control surface normal force derivative coefficient
C_m	pitching moment coefficient
C_{m_q}	pitch damping coefficient
C_X	axial force coefficient
C_{XC}	control surface axial force coefficient
D	diameter
\bar{I}, I_a, I_t	moment of inertia tensor, axial moment of inertia, transverse moment of inertia
GNC	guidance, navigation, and control
GPS	global positioning system

\bar{K}, \bar{P}	gain and solution to algebraic matrix Riccati equation for linear quadratic regulator controller
K_{PG}, K_{DG}	proportional and derivative gains for drift controller
L, M, N	moments acting on projectile
m	mass
M	Mach number
N_C	number of control surfaces
NC	non-control
p, q, r	body rotational velocity
$\dot{p}, \dot{q}, \dot{r}$	time rate of change of body rotational velocity
Q	dynamic pressure
$\bar{r}_{CG \rightarrow CPC}$	vector from center-of-gravity to center-of-pressure of control surface
\bar{R}, \bar{Q}_{LQR}	control effort and control error weighting matrix for linear quadratic regulator
S	reference area
t_{deploy}	control surface deployment time in flight
t_{glide}	glide start time in flight
u, v, w	body translational velocity
$\dot{u}, \dot{v}, \dot{w}$	time rate of change of body translational velocity
V	total velocity of projectile
$\dot{\bar{x}}, \bar{x}, \bar{u}$	time rate of change of state vector, state vector, control vector controller
x, y, z	inertial position
$\dot{x}, \dot{y}, \dot{z}$	inertial translational velocity
X, Y, Z	forces acting on projectile
y_T, z_T, \dot{y}_T	target inertial position and translational velocity for drift controller

NO. OF
COPIES ORGANIZATION

1
ELEC ADMNSTR
DEFNS TECHL INFO CTR
ATTN DTIC OCP
8725 JOHN J KINGMAN RD STE 0944
FT BELVOIR VA 22060-6218

3 US ARMY RSRCH LAB
ATTN IMNE ALC HRR
MAIL & RECORDS MGMT
ATTN RDRL CIO LL TECHL LIB
ATTN RDRL CIO MT TECHL PUB
ADELPHI MD 20783-1197

1 DIRECTOR
US ARMY RESEARCH LAB
RDRL D
2800 POWDER MILL RD
ADELPHI MD 20783-1197

NO. OF
COPIES ORGANIZATION

6 RDECOM ARDEC
RDAR MEF E
D CARLUCCI
M HOLLIS
C STOUT
A SANCHEZ
R HOOKE
J MURNANE
BLDG 94
PICATINNY ARSENAL NJ 07806-5000

8 RDECOM ARDEC
RDAR MEF S
D PANHORST
G MINER
N GRAY
R FULLERTON
B DEFRANCO
M MARSH
P FERLAZZO
D PASCUA
BLDG 94
PICATINNY ARSENAL NJ 07806-5000

4 RDECOM ARDEC
RDAR MEM C
D NGUYEN
R GORMAN
D CIMORELLI
K SANTANGELO
BLDG 94
PICATINNY ARSENAL NJ 07806-5000

3 RDECOM ARDEC
D DEMELLA
P MAGNOTTI
A LICHTENBERG-SCANLAN
BLDG 61S
PICATINNY ARSENAL NJ 07806-5000

2 RDECOM ARDEC
RDAR MEM M
C MOEHRINGER
J TRAVAILLE
BLDG 94
PICATINNY ARSENAL NJ 07806-5000

4 RDECOM ARDEC
RDAR MEM A
E VAZQUEZ
T RECCHIA
G MALEJKO
W KOENIG
BLDG 94S
PICATINNY ARSENAL NJ 07806-5000

NO. OF
COPIES ORGANIZATION

3 RDECOM ARDEC
J GRAU
W TOLEDO
S CHUNG
BLDG 95
PICATINNY ARSENAL NJ 07806-5000

3 RDECOM ARDEC
RDAR MEF I
R GRANITZKI
J CHOI
L VO
BLDG 95
PICATINNY ARSENAL NJ 07806

1 RDECOM ARDEC
RDAR MEM C
M LUCIANO
BLDG 65S
PICATINNY ARSENAL NJ 07806

1 US ARMY ARDEC
PROPULSION INDIRECT FIRE BR
RDAR MEE W
J LONGCORE
BLDG 382
PICATINNY ARSENAL NJ 07806

1 RDECOM ARDEC
RDAR MEF
M HOHIL
BLDG 407
PICATINNY ARSENAL NJ 07806-5000

4 RDECOM ARDEC
AMSRD AMR SG SD
J BAUMAN
H SAGE
S DUNBAR
B NOURSE
BLDG 5400
REDSTONE ARSENAL AL 35898

2 PM CAS
SFAE AMO CAS
R KIEBLER
P MANZ
BLDG 171
PICATINNY ARSENAL NJ 07806

2 PM CAS
SFAE AMO CAS EX
J MINUS
M BURKE
BLDG 171
PICATINNY ARSENAL NJ 07806

NO. OF
COPIES ORGANIZATION

2 PM MORTAR SYS
SFAE AMO CAS MS
P BURKE
G SCHWARTZ
BLDG 162S
PICATINNY ARSENAL NJ 07806-5000

1 PM MAS
SFAE AMO MAS
C GRASSANO
BLDG 354
PICATINNY ARSENAL NJ 07806

1 PM MAS
SFAE AMO MAS LC
D RIGOGLIOSO
BLDG 354
PICATINNY ARSENAL NJ 07806

1 PM MAS
SFAE AMO MAS SETI
J FOULTZ
BLDG 354
PICATINNY ARSENAL NJ 07806

1 FIRES DEPUTY MGR
EXP MANEUVER WARFARE
OFC OF NAVAL RSRCH
ONR 30
875 NORTH RANDOLPH ST
RM 1155B
ARLINGTON VA 22203

2 NAVAL SURFACE WARFARE CTR
DAHLGREN DIVISION
N COOK
L STEELMAN
6210 TISDALE RD STE 223
DAHLGREN VA 22448-5114

1 ALLIANT TECHSYSTEMS INC
R DOHRN
MN07-MN14
4700 NATHAN LANE N
PLYMOUTH, MN 55442

1 ALLIANT TECHSYSTEMS INC
ALLEGANY BALLISTICS LAB
S OWENS
MS WV01 08 BLDG 300 RM 180
210 STATE RTE 956
ROCKET CTR WV 26726-3548

NO. OF
COPIES ORGANIZATION

1 SAIC
J NORTHRUP
8500 NORMANDALE LAKE BLVD
STE 1610
BLOOMINGTON MN 55437-3828

1 SAIC
D HALL
1150 FIRST AVE STE 400
KING OF PRUSSIA PA 19406

1 GEN DYNAMICS ST MARKS
H RAINES
PO BOX 222
SAINT MARKS FL 32355-0222

1 GEN DYNAMICS ARM SYS
J TALLEY
128 LAKESIDE AVE
BURLINGTON VT 05401

3 BAE ARM SYS DIV
T MELODY
J DYVIK
B GOODELL
P JANKE
CO QUORTRUP
4800 E RIVER RD
MINNEAPOLIS MN 55421-1498

1 US ARMY YUMA PROVING GROUND
TEDT YPY MW
M BARRON
301 C STREET
YUMA AZ 85365-9498

1 TRAX INTRNTL CORP
R GIVEN
US ARMY YUMA PROVING GROUND
BLDG 2333
YUMA AZ 85365

1 ARROW TECH ASSOC
W HATHAWAY
1233 SHELBURNE RD
STE D-8
SOUTH BULINGTON VT 05403

1 GEORGIA INST OF TECHLGY
SCHOOL OF AEROSPACE ENG
M COSTELLO
ATLANTA GA 30332

NO. OF
COPIES ORGANIZATION

NO. OF
COPIES ORGANIZATION

ABERDEEN PROVING GROUND

6 COMMANDER
US ARMY TACOM ARDEC
AMSRD AR AEF D
R LIESKE
J MATTS
A SOWA
J FONNER
M ANDRIOLO
B NARIZZANO

45 DIR USARL
RDRL WM
P PLOSTINS
RDRL WML
M ZOLTOSKI
J NEWILL
RDRL WML A
W OBERLE
R PEARSON
L STROHM
RDRL WML D
J SCHMIDT
M NUSCA
RDRL WML E
I CELMINS
G COOPER
J DESPIRITO
L FAIRFAX
F FRESCONI (5 CPS)
J GARNER
B GUIDOS
G OBERLIN
J SAHU
S SILTON
P WEINACHT
RDRL WML F
F BRANDON
T BROWN
B DAVIS
T HARKINS
D HEPNER
M ILG
G KATULKA
D LYON
J MALEY
R MCGEE
C MILLER
P MULLER
P PEREGINO
D PETRICK
B TOPPER
RDRL WML G
W DRYSDALE
M MINNICINO

J BENDER
RDRL WML H
M FERMER-COKER
R SUMMERS
RDRL WML F
N GNIAZDOWSKI
R BITTING

INTENTIONALLY LEFT BLANK.